Contents lists available at ScienceDirect

Engineering Failure Analysis

journal homepage: www.elsevier.com/locate/engfailanal

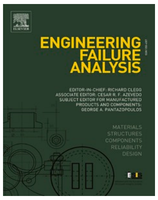

Corrosion – creep behavior of high – chromium nickel-based superalloys in the accelerated marine-atmospheric environment

Jianglong Ma[a], Guangming Kong[b], Keren Wang[c,d], Zhiguo Liu[b], Lin Zhao[e], He Yang[a], Chuangwei Liu[f,*], Ang Tian[a,*], Yiwei Wang[c,d,*]

[a] *School of Metallurgy, Northeastern University, Shenyang, Liaoning 110819, China*
[b] *Naval Aviation University Qingdao Campus, Qingdao, Shandong 266041, China*
[c] *Liaoning Province Key Laboratory for Phenomics of Human Ethnic Specificity and Critical Illness, Shenyang Medical College, Shenyang, Liaoning 110034, China*
[d] *Department of Molecular Morphology Laboratory, School of Basic Medicine, Shenyang Medical College, Shenyang, Liaoning 110034, China*
[e] *Institute of Metal Research, Chinese Academy of Sciences, Shenyang Liaoning 110016, China*
[f] *School of Software Engineering, Suzhou Institute for Advanced Research, University of Science and Technology of China, Suzhou, Jiangsu 215123, China*

ARTICLE INFO

Keywords:
K4648
Accelerated corrosion
Marine-atmospheric environment
Creep fracture surface
Creep mechanism

ABSTRACT

The influence of the accelerated marine atmospheric environment on the corrosion and mechanical properties of the K4648 alloy was investigated with electrochemical and creep tests in this work. The results show that the K4648 alloy is covered by Al_2O_3, Cr_2O_3, NiO, $NiCr_2O_4$, and Fe_2O_3 in the marine atmospheric environment. After accelerated corrosion, corrosion pits emerged on the alloy surface, accompanied by a decrease in the alloy's corrosion potential from − 154.23 mV to − 401.75 mV, an increase in the corrosion current density from 0.0037 μA/cm2 to 0.0733 μA/cm2, an approximate 60 % reduction in the thickness of the passive film. The creep life drops substantially, and under a stress of 80 MPa, the steady – state creep rate increases by 73 times compared to that before corrosion. In addition, the creep mechanism changes from being jointly dominated by diffusion and dislocations before corrosion to being dominated by dislocations. This study reveals the relationship between the long – term marine atmospheric environment and both the corrosion and creep behaviors of the K4648 alloy, and highlights the corrosion in the marine atmospheric environment which should be regarded as a core challenge that must be overcome for superalloys under actual working conditions.

1. Introduction

Nickel-based superalloys K4648 are widely used in the turbine blades of aero – engines and industrial gas turbines due to their excellent mechanical properties and environmental resistance at high temperatures. [1–3] However, the blades are failed premature failure under combined effects of environmental factors in work conditions, such as high temperature, and mechanical forces, chiefly including centrifugal force, aerodynamic force, and vibration force. [4–6] In order to prevent the premature failure of materials under harsh conditions, understanding the creep properties of materials is of vital importance for the stable operation of turbine blades. [4].

The hot-corrosion study and the creep-property research of alloys was investigated in the early research. [2,4,7–9] The main reason

---

* Corresponding authors.
E-mail addresses: cwliu@dicp.ac.cn (C. Liu), tiana@smm.neu.edu.cn (A. Tian), wangyiwei@symc.edu.cn (Y. Wang).

https://doi.org/10.1016/j.engfailanal.2025.110091
Received 17 July 2025; Received in revised form 23 August 2025; Accepted 5 September 2025

is that engines operating in a marine environment have a large number of salt deposits on the engine surface, mainly sourced from salt deposition in the atmosphere and the transformation of compounds in the fuel. [10] The types of salts mainly include chlorides, sulfates and vanadium pentoxide, and these salts deposited on the alloy surface can cause severe hot corrosion with the high temperature. [7] Research on creep properties mainly encompasses the impact of crystal orientation, element addition amounts, and microstructure on creep life. [1,11–13] Yang et al. studied the corrosion-creep behavior of nickel-based alloys at 900 °C under different stresses, and the results showed that hot corrosion weakened the alloy's deformation resistance, reduced the effective stress − bearing area, and decreased its creep performance. [4] Liu et al. [14] studied the creep properties of DD6 nickel − based alloy under molten − salt corrosion. The results showed that the failure of the specimen was due to the surface micro − cracks caused by corrosion. In 2023, Liu et al. [15] further studied the failure mechanism of nickel − based single − crystal superalloys under different molten − salt corrosion. It was found that the presence of sodium sulfate would reduce the effective area of the material, increase the true stress, and lead to creep failure. Homaeian et al. [16] studied the creep behavior of Alloy 617 under hot − salt corrosion and found that hot corrosion led to the formation of intergranular voids and oxides, which further caused creep failure. Therefore, for creep failure under hot − salt corrosion conditions, it is mainly due to the generation of micro − cracks, the reduction of the effective cross − sectional area, and intergranular voids within the alloy. Due to the hot corrosion problem of engines, which requires regular engine cleaning, the simulation results obtained in accordance with the HB 20401——2016 standard can no longer meet the requirement for evaluating the corrosion resistance of materials in actual marine service environments. [17] However, the corrosive impact of the marine atmosphere on materials is significant.

According to statistics from the World Corrosion Organization, half of the corrosion damage stems from atmospheric corrosion. [18] In the atmospheric corrosion environment, due to the high salinity, high humidity, and strong radiation characteristics of the marine environment, marine atmospheric corrosion is prone to occur, [19] and thus a large number of studies have been carried out. [20–23] Mendoza et al. [21] investigated the corrosion behavior of SAE AISI C0908 steel in rural, industrial urban and marine atmospheric environments. The results indicated that the corrosion rate of the steel exposed to the marine atmospheric environment was the highest. Melchers' analysis of data on high − nickel alloys in marine and atmospheric environments in recent years showed that local corrosion tends to level off after rapid initial − few − year growth. [24] Guo et al. [25] studied the effect of 33 − year atmospheric corrosion on the strength of Q235 steel, with results demonstrating that corrosion pits formed by long − term corrosion significantly reduced its yield strength, ultimate strength, elastic modulus, and ductility. Lin et al. [26] studied the influence of marine atmospheric corrosion on the mechanical properties of 2XXX Al − Li alloy, and the study revealed that intergranular corrosion and surface corrosion pits reduced the alloy's tensile strength. Tian et al. [27] studied the mechanical properties of 2524 − T3 aluminum alloy in a marine atmospheric environment, and showed that the reduction in the alloy's effective area led to a decline in its mechanical properties. The reasons for the degradation of mechanical properties and material failure of alloys in a marine atmospheric environment are mainly intra − granular corrosion, [26,28,29] reduction in the effective area, [27] and formation of corrosion pits. [30] Therefore, studying the creep mechanical behavior of the corroded K4648 alloy is of great significance for its application as engine structural components in marine environments. The accelerated corrosion test environmental spectrum can effectively simulate the long − term corrosion behavior of alloys in the atmospheric environment through equivalent coefficients in different environments.

The accelerated corrosion test environmental spectrum is based on Faraday's law and the principle of equivalent corrosion damage. [31–33] It comprehensively takes into account the combined effects of chloride ions, sulfate ions, illumination, temperature, and humidity in the marine-atmospheric environment. [31] Through electrochemical tests of nickel-based alloys at different temperatures and pH, the relationships between corrosion factors and corrosion rates are refined, thus constructing the accelerated corrosion test environmental spectrum for nickel-based alloys. [32] Chromium, as a crucial element in nickel-based superalloys, can enhance the corrosion and oxidation resistance of these alloys. [34] The nickel-based superalloy K4648 with the highest chromium content at present, has excellent welding properties, higher cost-effectiveness compared to cobalt − based superalloys, and is widely used in aero − engine manufacturing. [35].

In this study, the 10 − year corrosion behavior of the nickel − based high − chromium alloy K4648, which is used as a material for engine structural components. The research background pertains to cast superalloys in the aviation field, and the component in question is the engine structural components in the aviation field, was simulated in the marine atmospheric environment by means of an accelerated environmental test spectrum. The surface and cross-sectional corrosion morphologies of the K4648 alloy before and after corrosion were investigated via scanning electron microscopy (SEM) combined with energy-dispersive spectroscopy (EDS). X-ray diffraction (XRD) and X-ray photoelectron spectroscopy (XPS) were adopted to analyze the corrosion products. And the potentiodynamic polarization and electrochemical impedance spectroscopy were employed to explore the electrochemical behavior of the K4648 alloy before and after accelerated corrosion. Furthermore, the creep properties of the alloy at 850 °C were evaluated by the creep life under different stresses. The fracture surface of creep rupture, the microstructure after creep rupture were analyzed, and the creep mechanisms of the alloy before and after accelerated corrosion were discussed. This research holds engineering guiding significance for the application of nickel-based superalloys in a marine-atmospheric environment.

2. Methods and Experiments

2.1. Specimen preparation

The K4648 alloy was prepared via the triple-vacuum arc melting method. The chemical composition of the alloy was determined using inductively coupled plasma mass spectrometry (ICP-MS), as shown in Table S1. Subsequently, solution and aging treatments were carried out. The treatment procedures for these processes were: 1180 °C × 4h / AC (air cooling) + 900 °C × 6h / AC. [36].

2.2. Accelerated environmental test spectrum

In the marine atmospheric environment, nickel-based superalloys are mainly affected by temperature, moisture, and corrosive media. The accelerated corrosion test is carried out in a cyclic immersion corrosion test chamber (KLD-1200, Guangdong, China). An environmental acceleration spectrum is constructed through the principle of equivalent damage to accelerate the corrosion of the K4648 alloy. Yuan et al. [37] demonstrated that the corrosion of steel wires in a test environment with pH = 3.7, T = 50 °C, and a 5 % mass fraction of NaCl for 33.8 h is equivalent to one year of corrosion in the actual service environment. In this study, the annual action time of rainfall, sunlight, temperature, humidity, and fog water is converted into conditions of a 5 % NaCl solution with a pH of 4 and air with a temperature of 40 °C and a humidity of 90 %. Calculations based on the principle of equivalent damage indicate that corrosion for 78.17 h under these conditions is equivalent to one year of corrosion in the actual service environment. Statistics of the marine atmospheric environment in the past five years show that the average number of dry − wet alternations is 335, with a dry − wet time ratio of 6. Therefore, the time for a single cycle is 14 min, with the immersion test in the first stage lasting 2 min and the damp – heat test in the second stage lasting 12 min. The environmental conditions, relative humidity, and accelerated corrosion solution in the cyclic immersion corrosion test chamber are shown in Fig. S1. The accelerated corrosion test is composed of 10 periods, with forming a cycle, and 335 cycles constituting a period to simulate the alloy's corrosion in the real marine atmospheric environment for one year. The cyclic immersion test chamber for accelerated corrosion and the test cycle process are shown in Fig. S2. After the accelerated corrosion test, the corrosion morphology and corrosion products are characterized. The alloy after accelerated corrosion will be further subjected to electrochemical tests and creep tests to characterize the impact of marine atmospheric corrosion on the alloy's service. The accelerated corrosion test was carried out in an accelerated corrosion test chamber. There are two sizes of specimens used for the accelerated corrosion test. The first type, with a bottom diameter of 10 mm and a length of 50 mm, is for observing the corrosion morphology and corrosion products as well as for the electrochemical test after the corrosion test. The size of the second type, which is used for the creep test, will be introduced in Creep test.

2.3. Electrochemical tests

To further explore the corrosion properties of the K4648 alloy before and after accelerated corrosion, potentiodynamic polarization and electrochemical impedance spectroscopy (EIS) measurements were carried out using a Gamry reference 600 electrochemical workstation. For the electrochemical tests, cut 4-mm sections from the head part of the K4648 round bars, both before and after accelerated corrosion. The electrochemical test specimens were cylinders with a bottom diameter of 10 mm and a length of 4 mm. To ensure good electrical conductivity of the specimens, the backside of the electrochemical specimens was welded with copper wires, and the non-testing areas were sealed with epoxy resin. A three-electrode system was adopted for the electrochemical tests, consisting of a working electrode (the K4648 alloy specimens before and after accelerated corrosion), a saturated calomel reference electrode, and a counter platinum electrode. Before the electrochemical tests, the test specimens were cleaned in alcohol for 5 min to ensure a grease-free surface. The electrochemical test solution was a 3.5 % NaCl solution, with the temperature maintained at 25 ± 1 °C. During the electrochemical tests, the test samples were placed in the test solution for 30 min to stabilize the reaction system. The scanning rate of potentiodynamic polarization was 0.5 mV/s, and the frequency range of EIS tests was from 10^6 to 10^{-2} Hz with an amplitude of 10 mV. After the tests, the EIS data were analyzed using ZSimpWin software. All electrochemical tests were repeated at least three times to ensure accuracy.

2.4. Creep test

In order to explore the influence of the marine atmospheric environment on the creep properties of K4648 alloy, tensile creep tests were carried out at 850 °C using an electronic high − temperature creep testing machine (TSC105B). The equipment used for the creep test is shown in Fig. S3. In our tests, three kinds of stresses, 50 MPa, 60 MPa, and 80 MPa, were applied, which were determined from the yield strength of K4648 alloy at 850 °C. During the entire creep test process, the test temperature was controlled to be in a constant − temperature environment of 850 ± 2 °C by an electric resistance heating furnace. To ensure uniform heating of the material, the test specimen was heated to 850 °C at a heating rate of 5 °C / min and held for 30 min to stabilize the temperature in the gauge section. The variation of strain with time was collected using the TestPilot_HTC_D01C version 1.0.1106 data acquisition and control software. The creep specimen used in the experiment, along with its dimensions, is shown in Fig. S4. The diameter is 5 mm, the gauge length is 25 mm, and the total length of the specimen is 75 mm. [38] Before the creep test, the specimens were cleaned with acetone and dried, and the test ended when the specimens fractured.

2.5. Microstructure characterization

The microstructure of the heat − treated materials was observed using a scanning electron microscope. The element distribution and the elemental content of each phase were determined by an energy − dispersive spectrometer (EDS, OXFORD XMAX 20, Britain, UK). For the corroded specimens, the surface and cross − sectional morphologies were observed by a scanning electron microscope (FE-SEM, JEOL JSM-7800F, Tokyo, Japan), and the possible components of the corrosion products were analyzed and judged in combination with EDS. The phase and chemical state of the corrosion products were analyzed by an X-ray diffractometer (XRD, Rigaku SmartLab 9Kw, Tokyo, Japan) and an X - ray photoelectron spectrometer (XPS, Shimadzu Axis Supra+, Tokyo, Japan). In the XRD test, Cu was used as the target, and the diffraction patterns were collected in the range of $2\theta = 30^\circ - 80^\circ$ at a scanning rate of 10°/min. The

XPS data were peak – fitted using XPSpeak4.1 software. Before analysis, the energy was calibrated with the C1s peak at 284.5 eV as the internal standard. After the fracture surface of the specimen after creep fracture was ultrasonically cleaned in alcohol for 5 min, the fracture morphology was observed by SEM to determine the fracture mode. Additionally, the microstructure 3 mm below the fracture surface was observed by FE-SEM to analyze the microstructural evolution in the fracture area. All samples for microstructure observation were polished with a series of sandpapers and then with silica sol. Finally, they were chemically etched with a mixed solution of 50 mL HCl + 50 mL H_2SO_4 + 10 g $CuSO_4$ for 10 s to highlight the microstructural features of the materials.

3. Result and discussion

3.1. Microscopic structure

The microstructure of the heat-treated K4648 alloy was characterized by SEM, as shown in Fig. 1. The K4648 consists mainly of matrix γ phase, primary α phase, MC, and $M_{23}C_6$ phase. The formation of the primary phase is caused by the continuous segregation of Cr element in the residual liquid phase during the solidification process. Small-sized α phase starts to dissolve and large–sized α phase will transform into $M_{23}C_6$ when the solution temperature is higher than 1180 °C. For the K4648 alloy, the formed $M_{23}C_6$ phase is by the in-situ carbon absorption of the α phase, with the formation reaction being: $\alpha + C \rightarrow M_{23}C_6$. [35] The $M_{23}C_6$ phase formed is located between the α-phases in Fig. 1b, further indicating that $M_{23}C_6$ is formed by the in-situ absorption of C element by the large α-phases. EDS results indicate that the MC phase mainly contains Cr, along with some dissolved elements such as Mo and W. The compositions of the α phase and the MC phase are shown in Table 1. The content of Cr element in the α phase exceeds 65 %, so the α phase can be denoted as α_{Cr}.

3.2. Corrosion morphology

The highly humid marine environment can cause a liquid film to form on the alloy surface, on which corrosive substances deposit and further form an electrolytic film. [39] When the electrolytic film comes into contact with the alloy, atmospheric corrosion occurs, leading to the destruction of the passive film and the formation of corrosion pits. The surface morphologies of the K4648 alloy before and after corrosion are presented in Fig. 2a, indicating that the K4648 alloy polished with sandpaper shows no corrosion marks on its surface prior to corrosion. However, numerous corrosion pits have emerged on the surface of the K4648 alloy after corrosion (Fig. 2b), suggesting the occurrence of pitting corrosion in the alloy. Pitting corrosion includes the formation and growth stages, and different stages exhibit different morphologies. [40] The size of corrosion pits is approximately 1–2 μm, and as the corrosion time lengthens, smaller pits aggregate into larger ones with a length of about 10 μm. The occurrence of pitting corrosion is consistent with that of nickel-based alloy turbine blades operating in a marine environment. [5] The excellent corrosion resistance of nickel-based superalloys

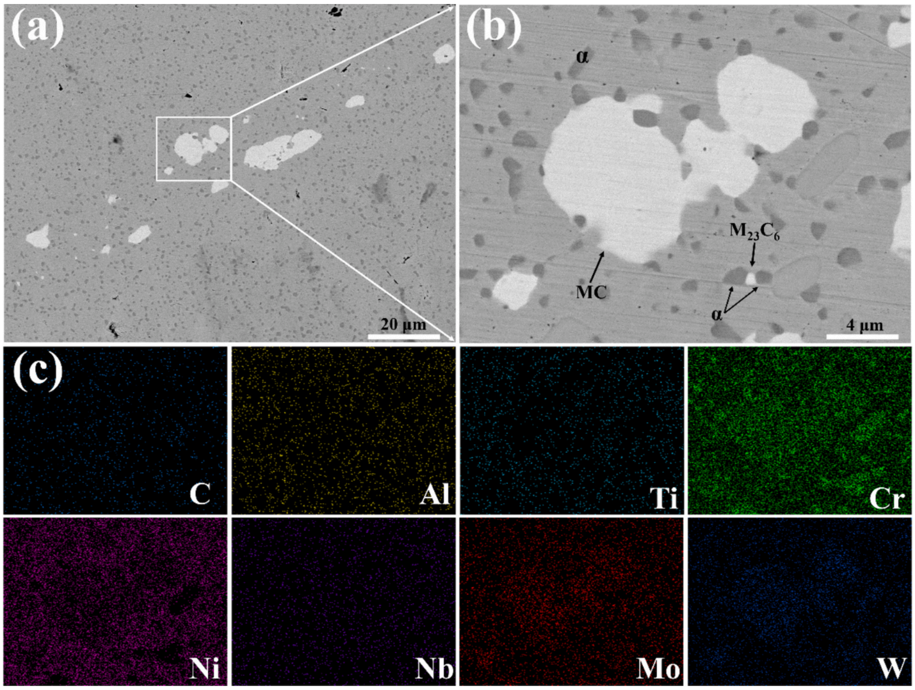

Fig. 1. The microstructure of K4648 alloy after heat treatment: (a) The overall microstructure of the alloy, (b) A partial enlarged view of (a), and (c) Element mapping diagram of (b).

Table 1
Chemical composition of α phase and $M_{23}C_6$ phase (wt. %).

Phase	C	Al	Ti	Cr	Ni	Nb	Mo	W
α	19.87	0.37	0.37	65.96	9.25	0.07	2.15	1.97
MC	26.99	0.10	0.22	39.33	24.17	0.21	4.94	4.04

is attributed to the dense oxide film formed on their surfaces. [41] EDS results indicate that there are no distinct oxide products on the surface of the K4648 alloy before corrosion. However, an aggregation of Al and O occurred at the large corrosion pits, suggesting that in the marine atmospheric environment after corrosion, the passive film of the K4648 alloy was damaged.

To further understand the impact of corrosion on the interior of the K4648 alloy, the cross-sections of the alloy before and after corrosion were examined by SEM. The cross-sectional morphologies of the K4648 alloy are presented in Fig. 2c and 2d. Fig. 2c indicates that there are no clearly corrosion pits on the K4648 alloy before corrosion. And corrosion pits with a certain depth emerged after corrosion in Fig. 2d. The average depth of the corrosion pits is 6 μm, suggesting that the corrosion rate of the K4648 alloy in the marine atmosphere is 0.6 μm/y. No intergranular voids or cracks, similar to those in the hot – salt corrosion of nickel – based alloys and the marine atmospheric corrosion of Al alloys, were observed inside the corrosion pits. This phenomenon indicates that the formed oxide film can effectively resist the intrusion of corrosive media. compared with the hot – salt corrosion of nickel – based alloys, the temperature of the marine atmospheric corrosion environment of nickel – based superalloys is lower, resulting in weaker chloride ion activity. [16] Meanwhile, compared with the marine atmospheric corrosion of Al alloys, the Al content in nickel – based alloys is lower. [42] Considering the surface and cross-sectional morphologies of the K4648 alloy, the protective oxide layer formed by the alloy in the marine atmospheric environment is thin, which differs from the hot corrosion of Ni-based superalloys. The hot corrosion of sample in molten salts results in a relatively thick oxide layer that, due to elemental competition, is divided into surface, middle and inner oxide films. [43,44] The primary reason for the differences in the oxide layers is the temperature disparity, with the temperature in the marine environment being far lower than that in the molten-salt hot-corrosion environment. No enrichment of O and other elements are observed inside the K4648 alloy, indicating that the oxide film formed in the marine atmospheric environment effectively hindered the diffusion of O into the alloy interior. The rapid formation of the oxide film benefits from the low activation energy of corrosion – resistant elements such as Al and Cr. [45].

3.3. Corrosion products

The XRD patterns of the corrosion products of the K4648 alloy before and after corrosion are demonstrated in Fig. S5. Before and after corrosion, the main corrosion products on the surface of the K4648 alloy are Al_2O_3, NiO, Cr_2O_3, and $NiCr_2O_4$. The oxidation of elements is related to their content and reactivity. As the Cl deposited on the metal surface is consumed over time, Ni reacts with the

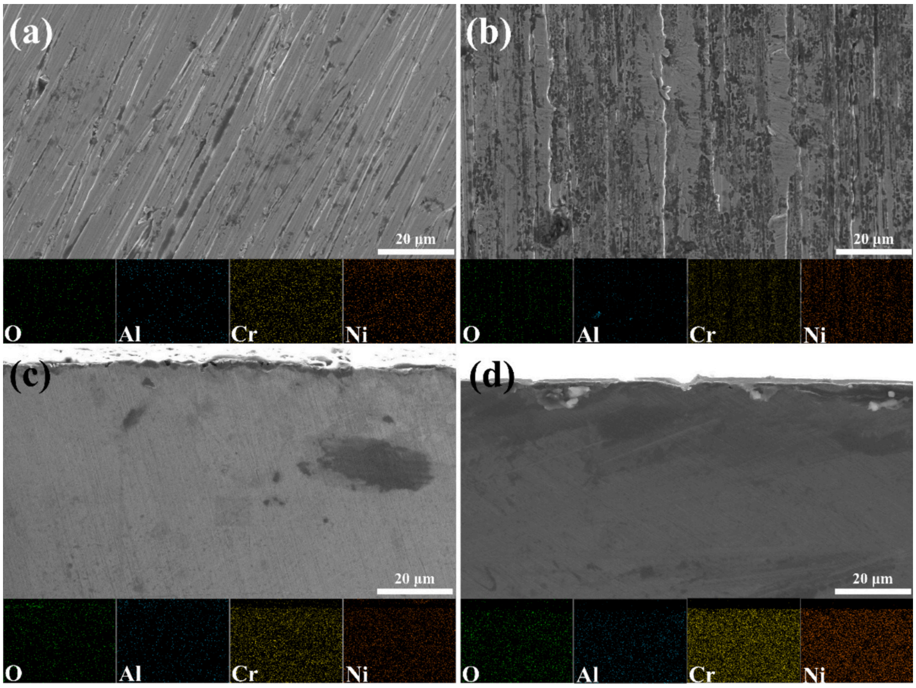

Fig. 2. The morphology of K4648 alloy before (a, c) and after (b, d) corrosion: (a, b) Surface morphology; (c, d) Cross – sectional morphology.

Cr_2O_3 formed on the surface to form $NiCr_2O_4$. [20] Subsequently, with the consumption of Cr, Al is further oxidized, [46] leading to the appearance of new characteristic peaks of $NiCr_2O_4$ and Al_2O_3 on the surface of the corroded metal.

To further analyze the oxide films before and after corrosion, XPS analyses of Al, Cr, Ni, and Fe on the surface and cross − section of the alloy before and after corrosion were carried out. Fig. 3a1-d1 show the Al 2p spectra. For the K4648 alloy, both the surface and cross-sections before and after corrosion exhibit two main peaks, corresponding to metallic Al (71.80 eV) and aluminum Al_2O_3 respectively. [47] The peak area of Al_2O_3 is much larger than that of metallic aluminum, indicating that Al mainly exists in the form of Al_2O_3.Calculations based on the XPS results show that the content of Al_2O_3 on the surface and cross-sections of the K4648 alloy before corrosion, as well as on the cross-sections after corrosion, is less than 85 %. However, the content of Al_2O_3 on the surface of the alloy after corrosion is higher than 95 %. The increase in the content of Al_2O_3 on the surface of the alloy after corrosion is consistent with the appearance of the characteristic peak of the (113) crystal plane of Al_2O_3 in the XRD results. The Cr 2p energy spectrum is presented in Fig. 3a2-d2, and the peak at around 573.84, 577.12, 587.01, and 538.38 eV correspond to metallic chromium (Cr), Cr_2O_3, $NiCr_2O_4$, and satellite peak, respectively. [47,48] For the K4648 alloy, before corrosion, Cr exists in the forms of metallic Cr, Cr_2O_3 and $NiCr_2O_4$ on both the surface and cross-section. After corrosion, Cr also has three forms in the cross-section. However, on the corroded metal surface, Cr mainly exists as Cr_2O_3 and $NiCr_2O_4$. This indicates that in the marine atmospheric environment, to resist the corrosion of corrosive media, the Cr element is oxidized to form Cr_2O_3.

The Ni 2p and Fe 2p energy spectrum are illustrated in Fig. 3a3-d3 and a4-d4 respectively. In the energy spectrum of the Ni element, there are mainly five peaks, corresponding to metallic Ni, [47] NiO, [49] $NiCr_2O_4$, [48] and the satellite peak of Ni $2p_{3/2}$ respectively.

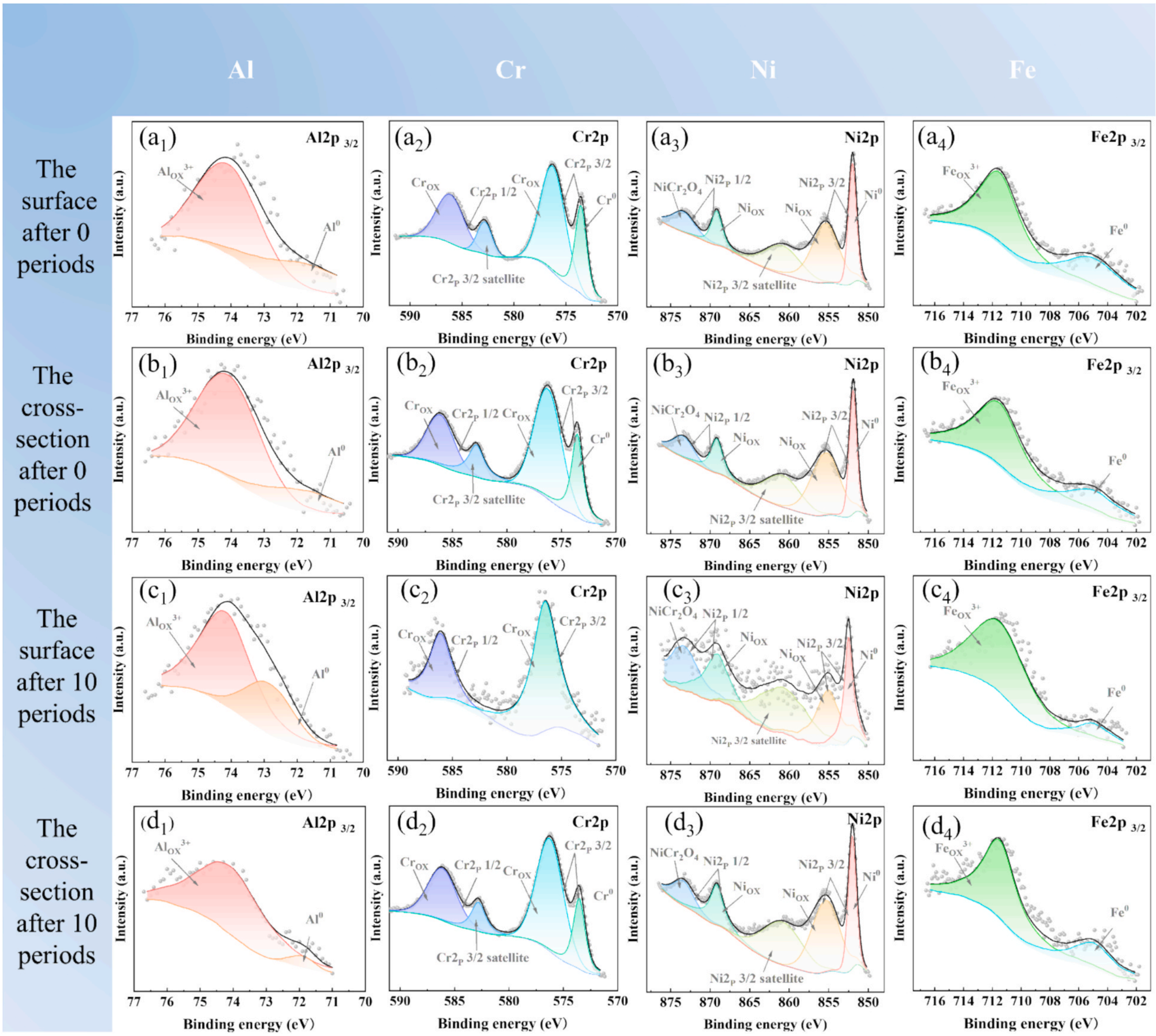

Fig. 3. XPS results of K4648 alloy on Al 2p, Cr 2p, Ni 2p and Fe 2p spectra before and after corrosion: (a_1-d_1) Al 2p; (a_2-d_2) Cr 2p; (a_3-d_3) Ni 2p; (a_4-d_4) Fe 2p.

[48,50] Fig. 3a3-d3 indicate that the forms of Ni element on the surface of the K4648 alloy are Ni, NiO, and $NiCr_2O_4$. Before corrosion, the content of $NiCr_2O_4$ on both the surface and cross-section, as well as that on the cross-section after corrosion, is less than 15 %. However, the content of $NiCr_2O_4$ on the surface of the alloy after corrosion is approximately 27 %. This indicates that as the corrosion progresses, the metallic Ni on the surface reacts with Cr_2O_3 to further generate $NiCr_2O_4$, [20] which is consistent with the appearance of the (222) crystal plane of $NiCr_2O_4$ on the surface after corrosion in the XRD pattern. In the Fe 2p energy spectrum, two peaks correspond to metallic Fe and Fe_2O_3. Then the Fe element change into Fe_2O_3 in the above sample. Combining the XRD and XPS analyses, the main corrosion products of the K4648 alloy after corrosion in the marine atmospheric environment are Al_2O_3, Cr_2O_3, NiO, $NiCr_2O_4$ and Fe_2O_3.

3.4. Electrochemical behavior

Potentiodynamic polarization curves can effectively characterize the corrosion behavior of alloys, such as pitting potential and active dissolution. [51] When the open-circuit potential reaches stability, the potentiodynamic polarization curves of the K4648 alloy before and after corrosion were measured as shown in Fig. 4a. Generally, the anodic reaction is considered to be the oxidation process of metals, while the cathodic reaction is the reduction process of oxygen. [52]

$$M \rightarrow M^{n+} + ne^{-} \tag{1}$$

$$O_2 + 4e^{-} \rightarrow 2O^{2-} \tag{2}$$

Where M represents the metals, and n refers to the number of transferred electrons.

Important parameters such as corrosion potential (E_{corr}), corrosion current density (I_{corr}), pitting potential (E_{pit}) and passive current density (I_{pass}) can be obtained from the potentiodynamic polarization curve to characterize the corrosion performance of materials. [53] The corrosion current density is obtained by extrapolating the Tafel polarization curve. The relevant parameters mentioned above are shown in Table 2. The value of E_{corr} is often used to represent the chemical inertness of an alloy. [54] The result indicate the sample has significantly corrosion- resistance. In other words, the higher E_{corr}, the lower the reactivity of the alloy and the stronger the corrosion resistance. And the corrosion potential of the K4648 alloy is decreased from −154.23 to −401.75 mV after corrosion, indicating a decline in the corrosion resistance of the K4648 alloy. The negative shift of E_{corr} is related to the increase in electroactive substances and ionic mobility, thus exacerbating the corrosion of the sample. The I_{corr} is employed to denote the corrosion rate of the alloy, while the E_{pit} is used to represent the alloy susceptibility to pitting corrosion. [55] A higher I_{corr} indicates a higher corrosion rate, making the alloy more liable to corrosion. Conversely, a higher E_{pit} implies lower susceptibility to pitting, rendering the alloy less likely to corrode via pitting. The increase of I_{corr} of K4648 alloy from 0.0037 μAcm^{-2} before corrosion to 0.0733 μAcm^{-2} and the decrease of

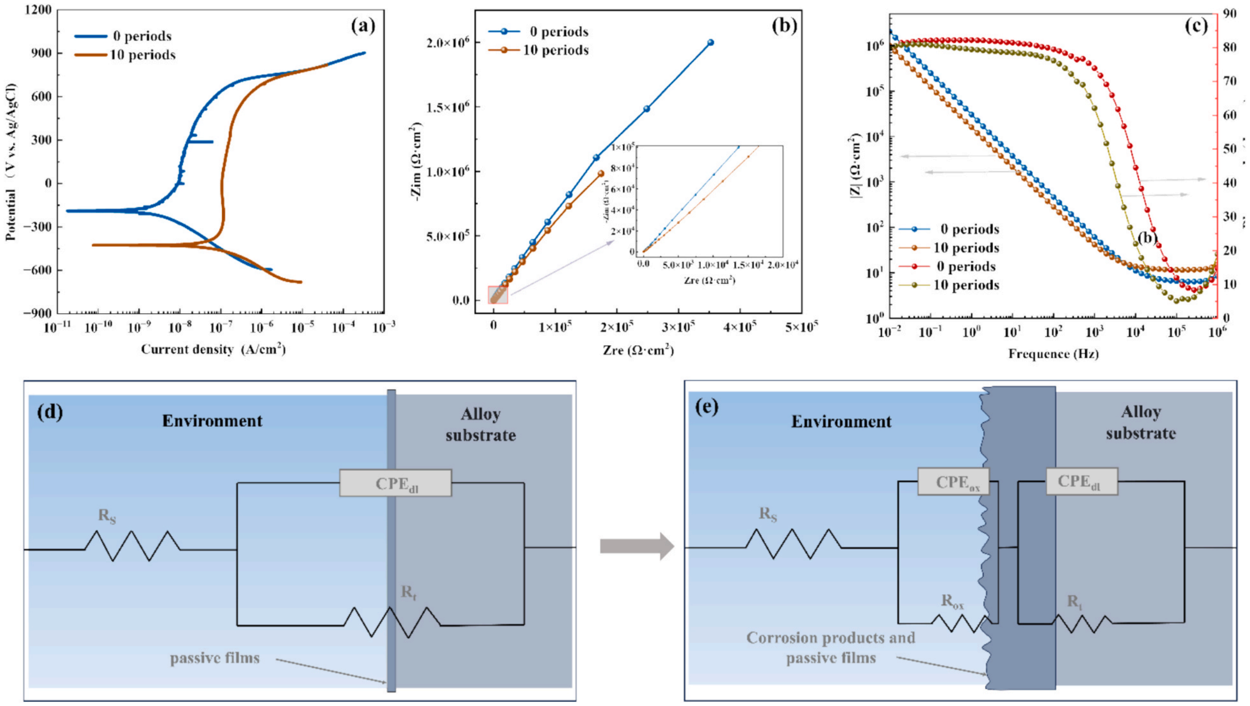

Fig. 4. Electrochemical properties of K4648 alloy before and after corrosion: (a) potentiodynamic polarization curves; (b) Nyquist plots; (c) Bode plots; (d) Equivalent circuit diagram before corrosion; (e) Equivalent circuit diagram after corrosion.

its E_{pit} from 694.16 to 634.62 mV indicate that the corrosion rate of K4648 alloy increases and its pitting-resistance performance declines after marine atmospheric corrosion. A high I_{pass} shows a high dissolution rate of the passive film, making the material prone to corrosion. The I_{pass} of the K4648 alloy increased from 0.0187 μAcm^{-2} before corrosion to 0.1302 μAcm^{-2}, indicating that the dissolution rate of the passive film on the surface of the K4648 alloy has increased and its corrosion resistance has decreased. Based on a comprehensive analysis of E_{corr}, I_{corr}, E_{pit}, and I_{pass} of the polarization curves of the K4648 alloy before and after corrosion, the corrosion resistance of the alloy decreases after accelerated corrosion in a marine atmospheric environment.

Electrochemical impedance spectroscopy is frequently used in the corrosion research of alloys to reveal reaction mechanisms and kinetics. [52] The Nyquist plots and Bode plots of the K4648 alloy are shown in Fig. 4b and c. The corrosion resistance of an alloy can be determined by the radius of the capacitive reactance arc, with a larger radius indicating stronger corrosion resistance. [56] The sample exhibits similar capacitive reactance arcs before and after corrosion. However, the radius of the capacitive reactance arc of the alloy after corrosion is smaller than that before corrosion, indicating a decrease in the corrosion resistance of the alloy after corrosion. The decrease in the alloy corrosion resistance is associated with the uneven corrosion pits formed on its surface, which result in surface non − uniformity along with the presence of pores and cracks. [57].

The Bode plots of the K4648 alloy before and after corrosion are shown in Fig. 4c. The corrosion resistance of high-chromium alloys mainly comes from the passive film formed on the alloy surface, whose performance can be represented by the impedance modulus $|Z|$ in the low-frequency region as it approaches 0. [58] The alloy exhibits good corrosion resistance, but the corrosion resistance of the alloy after corrosion is lower than that before corrosion. In the high-frequency region, the impedance modulus of the alloy before corrosion is lower than that of the alloy after corrosion, which may be caused by the cracking or shedding of the corrosion layer. [59] Typically, the wider the range of the peak phase angle, the more stable passive film of the alloy, the more difficult the charge transfer. [60] Within the frequency range of 10^{-2} to 10^{5}, the phase angle of the alloy after corrosion is always covered by that of the alloy before corrosion, indicating that the passive film formed on the alloy after corrosion is unstable and the alloy is more prone to corrosion.

For an in − depth understanding of the changes in the electrochemical characteristics of alloys suffering from pitting corrosion in a simulated marine atmospheric environment, the equivalent circuit was used to simulate the EIS data of the K4648 alloy before and after corrosion, as summarized in Fig. 4d and e. When an oxide layer forms on the metal surface, the migration of ions in the oxide layer has a significant impact on the corrosion rate, and the oxide layer can be considered as an equivalent capacitor in series with the double-layer capacitance. [51] The equivalent circuit involves solution resistance (R_s), double-layer capacitance (CPE_{dl}), charge-transfer resistance (R_t), oxide layer capacitance (CPE_{ox}), and oxide layer resistance (R_{ox}). Owing to the complexity of the environment and the non-uniformity of the specimen surface, a constant phase element (CPE) is often used in place of a capacitor to represent the capacitive characteristics of the double-layer at the interface between the measured electrode and the solution. [47] The impedance of the CPE is calculated by the following formula: [61]

$$Z_{CPE} = \frac{1}{Q(wi)^n} \tag{3}$$

Where Q is the CPE constant ($S^n \cdot \Omega^{-1} \cdot cm^{-2}$), representing the magnitude of the admittance; ω is the angular frequency (rad/s) with a value of 2πf, i is the imaginary unit ($i^2 = -1$); n is the fitting exponent defined as $n = \alpha (\pi/2)$ (α being the constant phase angle of the CPE). The value range of n is from 0 to 1, where $n = 0$ represents a pure resistor and $n = 1$ represents an ideal capacitor. [47,61]

The results in Table 3 indicate that the CPE_{dl} value of the K4648 alloy before corrosion is smaller than that after corrosion, suggesting that the corrosion resistance of the alloy before corrosion is higher than that after corrosion. The CPE_{dl} value is related to the active area participating in the electrochemical reaction. [62] A large number of corrosion pits on the alloy surface after corrosion increase the active area of the reaction, resulting in a decrease in its corrosion resistance. The R_t value is used to reflect the alloy's corrosion resistance, and the significantly lower R_t value of the alloy after corrosion compared to before further indicates a decline in the alloy corrosion resistance. After corrosion, a corrosion − oxidation layer forms on the alloy surface, which has some protective capacity for the alloy by impeding oxygen transport and ion transfer, so the total impedance of the corroded alloy can be represented as the sum of R_t and R_{ox}. However, the total impedance of the corroded K4648 alloy remains significantly lower than that of the uncorroded alloy, signifying a reduction in its corrosion resistance. The locally damaged oxide layer forms rapid-corrosion zones, reducing the alloy corrosion resistance. [51] Near the corrosion pits, the failure and non-repairability of the oxide film accelerate the corrosion rate, resulting in a decline in the alloy corrosion resistance. The fitted n-values, all greater than 0.7, indicate a high degree of agreement between the capacitor and the ideal capacitor. The order of χ^2 ranged from 10^{-5} to 10^{-3}, indicating that the fitting quality of the EIS data is satisfactory.

The corrosion resistance of the alloy is related to the thickness of the passive film formed on its surface, and the thicker the passive film, the less susceptible the alloy is to erosion by corrosive media, with the thickness of the passive film calculable by the following formula. [55]

Table 2

The electrochemical parameters of K4648 alloy before (0 periods) and after (10 periods) corrosion.

Specimens	E_{corr} (mV_{sce})	I_{corr} (μAcm^{-2})	E_{pit} (mV_{sce})	I_{pass}(μAcm^{-2})
0 periods	−154.23	0.0037	694.16	0.0187
10 periods	−401.75	0.0733	634.62	0.1302

Table 3
Equivalent circuit parameters of EIS data for K4648 alloy before and after corrosion.

Specimens	R_s ($\Omega.cm^{-2}$)	CPE_{dl} ($S^n.\Omega^{-1}.cm^{-2}$)	n_{dl}	R_t ($\Omega.cm^{-2}$)	CPE_{ox} ($S^n.\Omega^{-1}.cm^{-2}$)	n_{ox}	R_t ($\Omega.cm^{-2}$)	d nm	χ^2
0 periods	6.74	6.20×10^{-6}	0.90	1.84×10^{17}				4.11	5.80×10^{-3}
10 periods	11.75	1.23×10^{-5}	0.91	3.86×10^{7}	1.96×10^{-4}	0.73	1.40×10^{3}	1.62	3.76×10^{-5}

$$d = \frac{\varepsilon_0 \varepsilon A}{C_{eff}} \tag{4}$$

Where ε_0 represents the permittivity of free space (8.8541×10^{-14}F/cm), ε denotes the relative permittivity, A is the area of the specimen, and C_{eff} is the capacitance of the passive film that can be derived from the following Brug equation:

$$C_{eff} = CPE_{dl}^{\frac{1}{n}} \left(\frac{1}{R_s} + \frac{1}{R_t} \right)^{\frac{n-1}{n}} \tag{5}$$

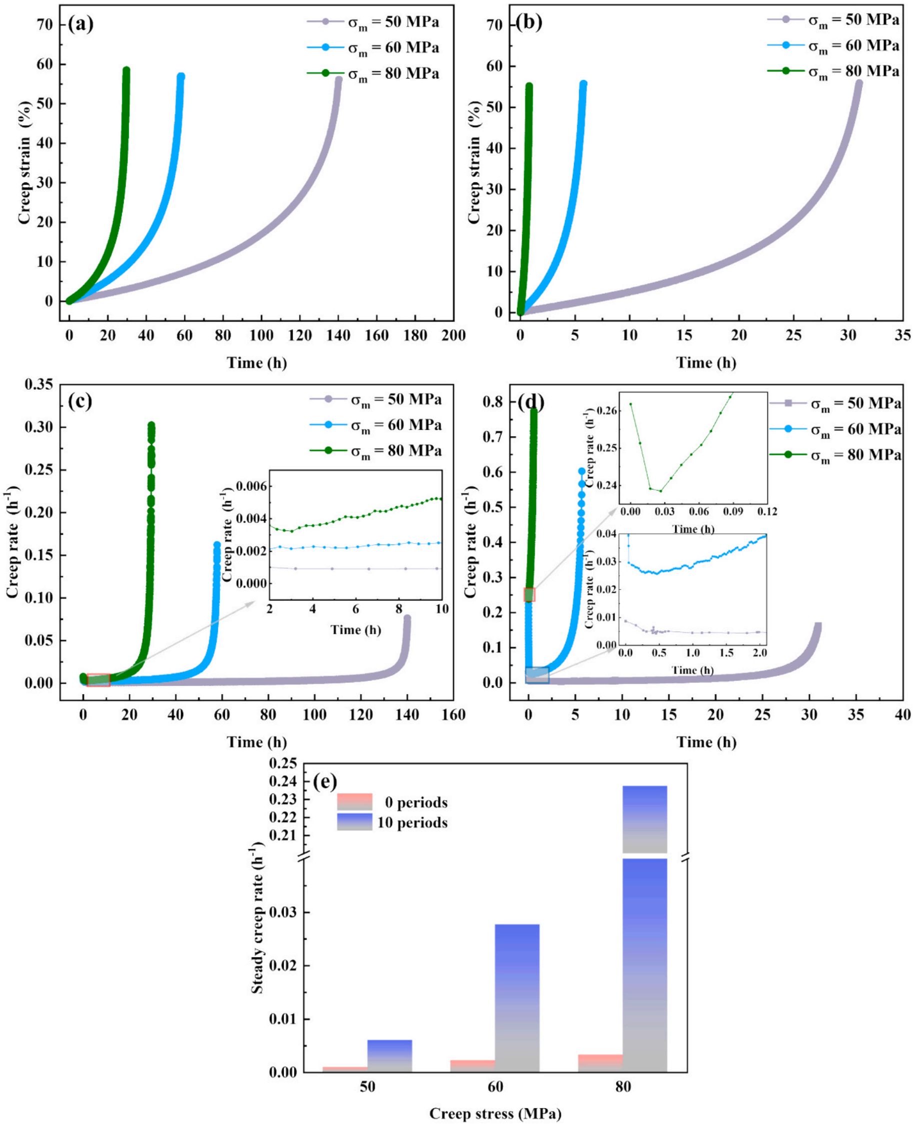

Fig. 5. The creep properties of the K4648 alloy before (a, c) and after (b, d) corrosion: (a, b) Creep curves; (c, d) Creep rate curves; (e) comparison diagram of steady − state creep rates before and after corrosion.

A thicker passive film helps prevent the occurrence of pitting corrosion, while areas with a thinner passive film are liable to be broken through by fluctuating stresses. [63] After corrosion, the thickness of the passive film on the surface of the K4648 alloy decreased from 4.11 nm before corrosion to 1.62 nm, indicating that the presence of corrosion pits is detrimental to the formation of the passive film on the surface, further reducing the corrosion resistance of the alloy. The formation of the passive film after corrosion is related to the Mo element. In engineering, the ability of an alloy to resist local corrosion can be measured by the pitting corrosion resistance equivalent (PRE). [64]

$$PRE = Cr + 3.3(Mo + 0.5W) + 16N \tag{6}$$

Generally, the higher the PRE value, the better the alloy's resistance to local corrosion. The PRE value of the K4648 alloy is 50.28. Although the thickness of the passive film has decreased after corrosion, it still provides certain protection to the alloy by impeding the corrosion of corrosive ions into the interior of the alloy. This is consistent with the cross – sectional morphology of the alloy after corrosion.

3.5. Creep behavior

In order to assess the influence of the marine atmospheric environment on the creep properties of the K4648 alloy, creep tests were conducted at 850 °C under three different stress conditions (50, 60, 80 MPa). Creep is a temperature-sensitive thermally activated process, which is generated by the combined effects of atomic thermal motion, dislocation movement, and stress. [65].

Fig. 5 shows the creep curves, creep rate curves, and steady-state creep rate diagrams of the K4648 alloy before and after corrosion. Fig. 5a and b indicate that at the same temperature, the greater the stress, the shorter the creep life. Interestingly, the stress has a significant impact on creep life. After the alloy is corroded by the marine atmosphere, its creep life drops sharply, being less than 1 h under a stress of 80 MPa. The creep life corresponding to the minimum stress after corrosion is nearly identical to that corresponding to the maximum stress before corrosion. This displays that the changes in the specimen surface morphology induced by marine

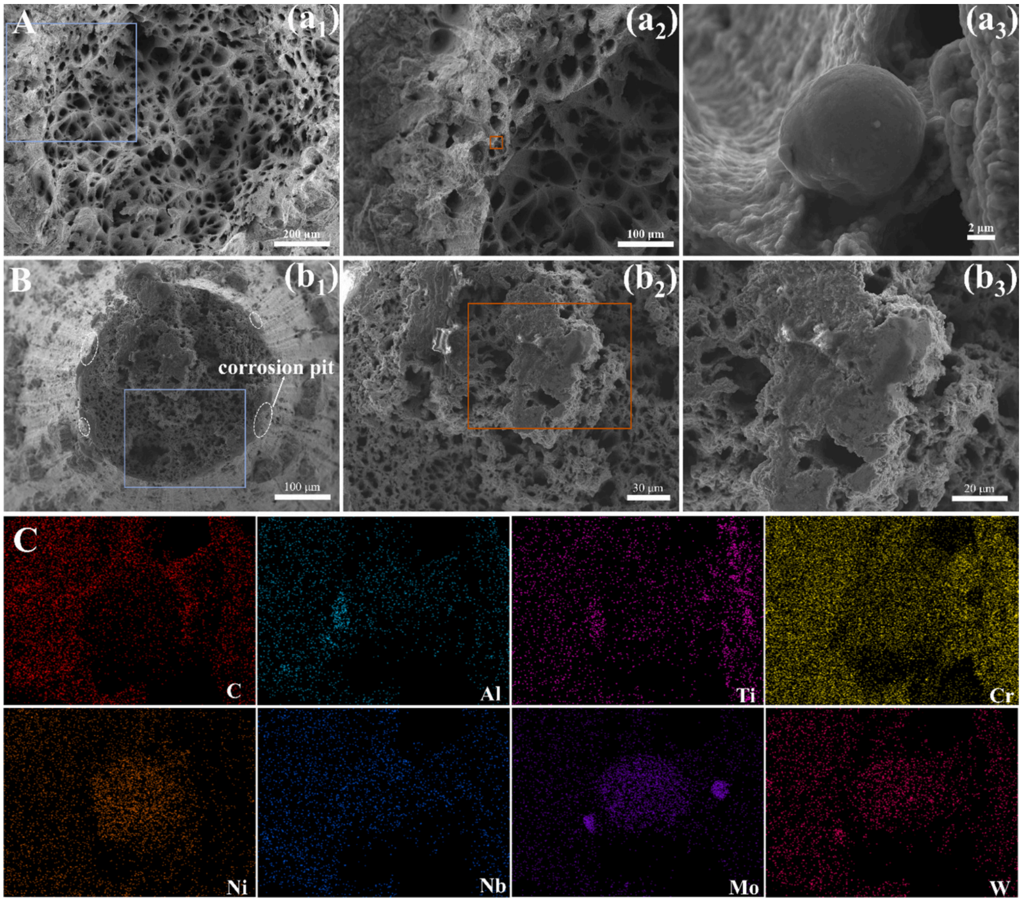

Fig. 6. Fracture morphology of the K4648 alloy before (A) and after (B) corrosion (50 MPa): (a$_1$ and b$_1$) Macrograph of fracture; (a$_2$ and b$_2$) Enlarged view of the blue area in (a$_1$ and b$_1$); (a$_3$ and c$_3$) Enlarged view of the orange – colored area in (b$_2$ and b$_2$); (C) Element mapping diagram of (a$_3$).

atmospheric corrosion have a substantial impact on creep life, highlighting that marine atmospheric corrosion cannot be overlooked. The creep curve generally consists of three stages, namely the primary creep stage, the steady-state creep stage, and the tertiary creep stage. There is no obvious decelerated creep stage after corrosion, and the creep curve mainly consists of the steady-state creep stage and the accelerated creep stage. The steady-state creep stage is a process of interaction between dislocations and obstacles, while the accelerated creep stage is a process of creep damage accumulation. [66].

The creep rate curves were used to understand the influence of marine atmospheric corrosion on the creep properties of the K4648 alloy, as illustrated in Fig. 5c and d. The alloy mainly exhibits a stage of constant rate and a stage of rate increase, which is consistent with the results of the creep curve. Before and after corrosion, as the creep stress increases, the minimum creep rate also increases, as shown in the enlarged views. Fig. 5e further indicates that the minimum creep rate of the corroded alloy is higher than that of the uncorroded alloy under the same stress conditions. This result confirms that marine atmospheric corrosion can significantly accelerate the creep rate. Especially, the steady-state creep rate of the corroded alloy is approximately 73 times higher than that of the uncorroded alloy under the condition of 80 MPa. The increase in the steady-state creep rate is attributed to the fact that atmospheric corrosion slightly reduces the load-bearing cross-sectional area of the creep specimen, thereby increasing the actual average stress.

The fracture of the K4648 alloy before corrosion (Fig. 6a1) indicates that the alloy undergoes necking behavior under the action of stress, which is consistent with the high elongation after fracture in the creep curve. Viewed comprehensively (Fig. 6a1, Fig. S6 a1 and b1), the fracture mode of the alloy prior to corrosion is mainly micro-void coalescence fracture, with the number of micro-voids increasing as the stress decreases. During the creep process, the formation of micro-voids is mainly caused by the connection of dimples within the matrix. [67] The amount of micro-voids can be used to judge the length of creep time. [68] Generally, the more micro-voids formed on the fracture surface, the better the creep performance of the alloy, which is consistent with the creep life results in Fig. 5a.

During creep process, stress induces the formation of dislocations, which then serve as diffusion pathways for elements, ultimately causing element diffusion and the formation of new compounds. [69] Fig. 6a3 indicates that two types of globular substances with different sizes precipitate in the K4648 alloy under different stresses before corrosion. In the large-sized globular substances, elements such as Cr, Ni, Mo, and W are enriched, while in the small − sized ones, the enrichment is mainly of Ti and Al. By comparing the enriched elements in the large-sized globular substances with those in the MC in the original structure of K4648 alloy, an additional Ni enrichment in the large-sized globular substances is found. The above-mentioned phenomena indicate that MC decomposes, with Ni elements in the matrix diffusing into MC and Ti and Al elements in MC diffusing into the matrix. High concentrations of Ti and Al promote the formation of the η-phase, yet the η-phase has limited solubility for elements such as Mo and W, causing Mo and W to precipitate adjacent to the η-phase. [70] Cai et al. found that the primary carbides of the alloy decompose under the influence of temperature and stress during the creep process and form the η − phase. [69] The creep behavior of the K4648 alloy before corrosion is controlled by element diffusion, leading to the formation of globular substances based on the MC and η-phases.

The creep fracture surface of the corroded K4648 alloy is shown in Fig. 6B. The fracture mode of the alloy changes from micro − void coalescence fracture before corrosion to being dominated by tear ridges, with the direction of the tear ridges perpendicular to the stress − loading direction. Fig. S6 C and D indicate that the transformation of the creep fracture mode under high − stress conditions (60 and 80 MPa) is more obvious compared with that before corrosion. Furthermore, Figs. S6 d2 and d3 indicate that cracks appear internally and further propagate towards the outer surface of the specimen, resulting in the specimen fracture. The corrosion pits on the specimen surface exacerbate oxidation, forming an oxide layer that reduces the effective area of the specimen and decreases its creep life. The corrosion pits formed under molten-salt hot-corrosion conditions are more severe because Cl^- reacts with O_2 and the surface metal, damaging the oxide layer. The infiltration of molten salt exacerbates corrosion, promotes crack propagation forward, and the specimen fracture originates from the specimen surface. [16] However, stress is transferred inwards along the pits in the presence of corrosion pits, resulting in stress concentration at the phase interface. Oxidation on the specimen surface causes the formation of oxidation vacancies which, under the influence of stress, move and aggregate to form voids and initiate cracks within the alloy. [71] Therefore, there are two main reasons for the reduction in creep life after corrosion: the decrease in the effective surface area of the specimen and the promotion of internal stress concentration in the alloy by surface corrosion pits. By comparing the morphologies of the fracture edges before and after corrosion (Fig. 6a1 and b1), it can be observed that the edges of the alloy are covered with dimples of various sizes before corrosion, but become smooth and flat after corrosion. The fracture before corrosion exhibits the characteristics of ductile fracture, while the alloy after corrosion shows the characteristics of brittle fracture. A more in − depth observation of the fracture edge after corrosion reveals the presence of corrosion pits. The defects of these corrosion pits can affect the stress distribution. The larger the corrosion pits are, the more likely stress concentration and transmission will occur, leading to premature failure of the material, [26,29,30] which is consistent with the results in Fig. 5.

During the creep process, the steady − state creep rate is controlled by temperature and stress. The constitutive equation of creep deformation is used to describe this relationship [72], as shown in the following formula:

$$\dot{\varepsilon}_s = A\sigma^n \exp\left(-\frac{Q}{RT}\right) \tag{7}$$

Where $\dot{\varepsilon}_s$ is the minimum creep strain rate (s^{-1}), A is the material constant, σ is the applied stress (Pa), n is the creep exponent, Q is the apparent activation energy for creep (J/mol), R is the universal gas constant (8.314 J/(mol·K)), and T is the absolute temperature (K).

The creep exponent n is often used to represent the creep mechanism. At a constant temperature, the following equation can be derived from Equation (7):

$$n = \left(\frac{\partial ln\dot{\varepsilon}}{\partial ln\sigma}\right)_T \tag{8}$$

Generally, n = 1 represents diffusion creep, n = 2——3 indicates that the process is controlled by diffusion and dislocation, n = 4–8 refers to dislocation creep. [73]

The relationship between the natural logarithm of the steady-state creep rate and stress of the K4648 alloy is summarized in Fig. 7. The results indicate that the creep is dominated by diffusion and dislocations before corrosion, while the creep mechanism is dislocation creep after corrosion. Fig. 6 also proves that during the creep process before corrosion, there is an inter-diffusion of elements, and the interaction between dislocations and precipitates leads to creep fracture. By contrast, the creep fracture of the alloy after corrosion is mainly caused by the interaction between dislocations and precipitates.

The microstructure beneath the creep fracture surface is presented in Fig. 8. Fig. 8a reveals that MC in the alloy decomposed during the creep process. Li et al. indicated that during the creep process, MC decomposes into $M_{23}C_6$ and the η phase is formed.[74] Spherical $M_{23}C_6$ can inhibits grain-boundary sliding through the pinning effect, thereby enhancing creep resistance, [75] which is consistent with the spherical precipitates on the fracture surface of the alloy before corrosion in Fig. 6. The η phase contributes to the formation of serrated grain boundaries during the creep process, regulating the creep stress, accommodating creep deformation, and delaying crack propagation. [76] Fig. 8b shows an enrichment of Ti beside the decomposed MC. A high Ti/Al ratio readily leads to the formation of the η phase. [77] Therefore, the creep of the K4648 alloy is controlled by elemental diffusion. Under the action of elemental diffusion, MC forms $M_{23}C_6$ and the η phase, which agrees with the results of Fig. 8.

Inside the microstructure of the K4648 alloy after creep fracture, a distinct crack can be observed, which is wider in the middle and tapers at both ends. It can be judged that the crack originated from the interior of the alloy and propagated outwards. This further indicates that stress is transferred inwards along the corrosion pits. Dislocations accumulated beside the α, entered the α through shearing, which further leds to the fragmentation of α. Subsequently, the crack propagated along the phase boundary, resulting in the failure of the specimen. The α in the K4648 alloy is a hard and brittle phase, making it difficult to absorb energy through plastic deformation. [36] Due to the rapid propagation of the crack, which led to a short creep-failure time, no obvious elemental diffusion behavior is detected.

4. Conclusions

In this paper, accelerated environmental test spectrum were employed to simulate the corrosion behavior of K4648 alloy in a marine atmospheric environment over a period of 10 years. Subsequently, electrochemical and creep tests were carried out to measure the properties of the alloy before and after corrosion. The conclusions are as follows:

Under the simulated marine atmospheric environment, the alloy undergoes pitting corrosion with corrosion products mainly being Al_2O_3, Cr_2O_3, NiO, $NiCr_2O_4$ and Fe_2O_3, and the unevenness of the alloy surface after corrosion causes an increase in corrosion current density and a decrease in corrosion resistance.

Before corrosion, the equivalent circuit of the alloy is mainly composed of double-layer capacitance, while after corrosion, it was composed of corrosion-layer capacitance in series with double-layer capacitance, and the thickness of the passive film formed on the alloy surface decreased from 4.11 nm before corrosion to 1.62 nm after corrosion, a 60 % reduction, which greatly reduced the corrosion resistance of the alloy.

After corrosion, the creep resistance of the alloy significantly decreased, with reduction rates of 78 %, 90 % and 98 % under the conditions of 50, 60 and 80 MPa respectively. The fracture surface before corrosion is composed of numerous micro-pores, while it was

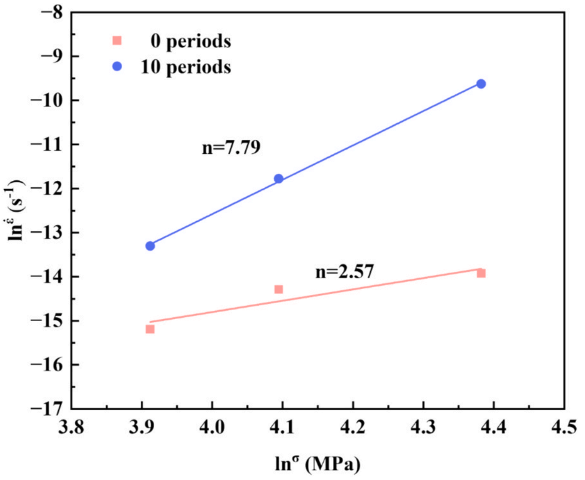

Fig. 7. The relationship between the steady-state creep rate and the logarithm of stress of K4648 alloy before and after corrosion.

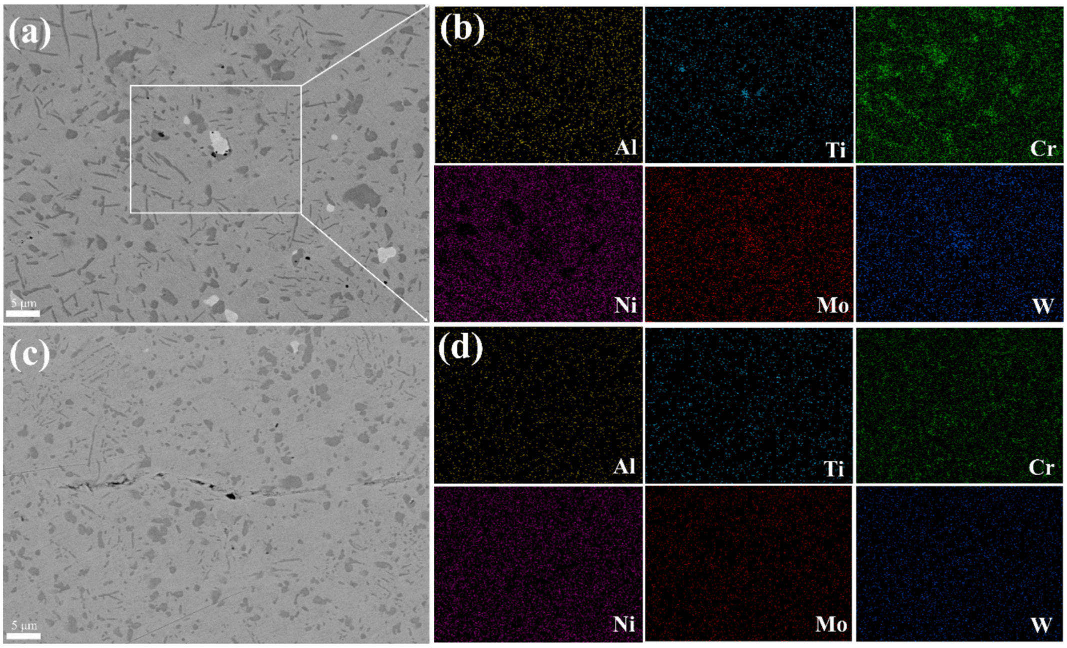

Fig. 8. Microstructure morphology under the creep fracture of K4648 alloy(50 MPa): (a, b) before corrosion (0 periods) and corresponding element mapping diagram of the white rectangular area; (c, d) after corrosion (10 periods) and corresponding element mapping diagram.

dominated by tear ridges after corrosion.

Before corrosion, during the alloy creep process, the decomposition of MC occurred. The creep mechanism shifted from being dominated by diffusion and dislocations before corrosion to dislocation-creep.

To prevent the reduction of material service life due to corrosion pits caused by long – term corrosion in a marine atmospheric environment, the following four aspects can be considered. Firstly, consider the alloy composition. The addition of Mo and W can effectively promote the formation of a passive film. By adjusting the contents of Mo and W and conducting electrochemical tests, the corrosion resistance of the alloy can be effectively studied. Secondly, the alloy properties can be regulated by considering the material forming method. Currently, some research has been done on preparing alloys through selective laser melting, but the preparation parameters need to be further optimized to improve material properties. Thirdly, the size of the alloy and the content and size of the second – phase particles can be adjusted by heat treatment processes. Fourthly, an anti – corrosion coating can be applied to the alloy surface to protect it. Thermal – sprayed ceramic coatings can effectively protect the alloy, reduce its corrosion, and extend its service life. For the alloys prepared by the first three methods, apart from considering the corrosion resistance of the materials, their mechanical properties should also be taken into account. The fourth method is simple and easy to implement, yet it requires regular maintenance. In the next stage, we will carry out experimental research on the gas – fired hot corrosion of alloys.

Data availability.

The raw/processed data required to reproduce these findings cannot be shared at this time as the data also forms part of an ongoing study.

CRediT authorship contribution statement

Jianglong Ma: Writing – original draft, Methodology, Formal analysis, Data curation, Conceptualization. **Guangming Kong:** Writing – review & editing, Methodology. **Keren Wang:** Methodology, Data curation, Conceptualization. **Zhiguo Liu:** Methodology, Formal analysis, Data curation. **Lin Zhao:** Methodology, Formal analysis, Data curation. **He Yang:** Project administration, Data curation, Conceptualization. **Chuangwei Liu:** Writing – review & editing, Methodology, Investigation. **Ang Tian:** Project administration, Methodology, Data curation, Conceptualization. **Yiwei Wang:** Project administration, Methodology, Funding acquisition, Conceptualization.

Declaration of competing interest

The authors declare that they have no known competing financial interests or personal relationships that could have appeared to influence the work reported in this paper.

Acknowledgments

Authors acknowledge the support from the Team Construction Project of Liaoning Province Education Department (Grant No. LJ222410164013), the Liaoning Provincial Natural Science Foundation (Grant No. 2024-MS-224), and the Basic Scientific Research Foundation of Central College (N2425015).

Appendix A. Supplementary data

Supplementary data to this article can be found online at https://doi.org/10.1016/j.engfailanal.2025.110091.

Data availability

The authors do not have permission to share data.

References

[1] H. Wang, X. Li, Y. Shang, S. Zhang, B. Hu, Y. Pei, S. Li, S. Gong, J. Mater. Res. Technol. 29 (2024) 3205–3216.
[2] J.H. Wang, D.G. Li, T.M. Shao, Corros. Sci. 200 (2022) 110247.
[3] Y. He, X. Liu, C. Xing, Z. Bian, Q. Zhou, J. Wang, H. Wang, J. Li, Prog. Nat. Sci.: Mater. Int. 32 (2022) 375–384.
[4] Y.Q. Yang, Y.C. Zhao, Z.X. Wen, J.J. Wang, M. Li, H.Q. Pei, Z.F. Yue, Mater. Sci. Eng. A 897 (2024) 146350.
[5] S. Han, J. Zhang, X. Lei, R. Yang, N. Wang, Corros. Sci. 217 (2023) 111111.
[6] S. Li, X. Yang, H. Qi, G. Xu, D. Shi, Mater. Sci. Eng. A 678 (2016) 57–64.
[7] V. Mannava, A.S. Rao, N. Paulose, M. Kamaraj, R.S. Kottada, Corros. Sci. 105 (2016) 109–119.
[8] X. Lu, X. Dai, K. Qi, C. Liu, S. Li, W. Qi, Appl. Surf. Sci. 648 (2024) 158833.
[9] S. Bagui, A.K. Ray, J.K. Sahu, N. Parida, J. Swaminathan, M. Tamilselvi, S.L. Mannan, Mater. Sci. Eng. A 566 (2013) 54–60.
[10] K.L. Luthra, H.S. Spacil, J. Electrochem. Soc. 129 (1982) 649.
[11] F. Leng, P. Lv, L. Liu, Y. Zhao, J. Zhang, Mater. Sci. Eng. A 915 (2024) 147272.
[12] N. Tian, G. Zhao, Z. Shi, B. Li, X. Shang, S. Zhang, H. Yan, J. Mater. Res. Technol. 29 (2024) 1350–1358.
[13] S. Lu, Z. Luo, F. Lu, L. Li, Q. Feng, J. Mater. Res. Technol. 29 (2024) 4870–4880.
[14] H. Liu, X.M. Wang, P.Y. Liu, Z.N. Zhao, W.Z. Yang, L. Li, Eng. Fract. Mech. 260 (2022) 108194.
[15] H. Liu, X.M. Wang, Z.N. Zhao, H.T. Li, W.Z. Yang, L. Li, Eng. Fail. Anal. 147 (2023) 107171.
[16] A. Homaeian, M. Alizadeh, Eng. Fail. Anal. 66 (2016) 373–384.
[17] W. Wang, Z. Yu, Y. Cui, R. Liu, L. Liu, S. Geng, F. Wang, J. Mater. Res. Technol. 22 (2023) 2316–2327.
[18] B. Chico, D. de la Fuente, I. Diaz, J. Simancas, M. Morcillo, Materials (basel) 10 (2017) 601.
[19] Y. Fan, W. Liu, S. Li, T. Chowwanonthapunya, B. Wongpat, Y. Zhao, B. Dong, T. Zhang, X. Li, J. Mater. Sci. Technol. 39 (2020) 190–199.
[20] Q. Sun, B. Zhang, D. Zhang, Y. Yang, J. Lin, F. Wang, Mater Charact 201 (2023) 112885.
[21] A.R. Mendoza, F. Corvo, Corros. Sci. 41 (1999) 75–86.
[22] I. Díaz, H. Cano, P. Lopesino, D. de la Fuente, B. Chico, J.A. Jiménez, S.F. Medina, M. Morcillo, Corros. Sci. 141 (2018) 146–157.
[23] B. Zhang, Y. Wang, H. Wan, J. Deng, W. Li, F. Liu, Eng. Fail. Anal. 154 (2023) 107684.
[24] R.E. Melchers, Corros. Rev. 38 (2020) 515–528.
[25] Q. Guo, Y. Zhao, Y. Xing, J. Jiao, B. Fu, Y. Wang, Structures 39 (2022) 115–131.
[26] L. Xiang, J. Tao, Q. Chen, Y. Wang, Y. Zhang, Y. Su, S. Chai, F. Zhang, X. Xia, J. Mater. Res. Technol. 26 (2023) 5838–5850.
[27] H. Tian, Z. Cui, B. Zhang, W. Yang, Y. Yang, H. Cui, Corros. Sci. 239 (2024) 112398.
[28] N. Li, X. Yan, X. Liu, L. Han, W. Zhang, Metals 12 (2022) 2173.
[29] L. Xiang, J. Tao, X. Xia, Z. Zhao, Q. Chen, Y. Su, S. Chai, Z. Zheng, J. Sun, Materials (basel) 16 (2023) 2396.
[30] L. Xiang, F. Li, X. Wu, F. Zhang, J. Tao, M. Wang, W. Lei, X. Ran, H. Wang, Materials 17 (2024) 5353.
[31] S.B. Xing, X.G. Li, L. Li, Adv. Mat. Res. 557–559 (2012) 50–53.
[32] R. Li, C. Miao, M. Nie, Y. Wang, Anti-Corros. Methods Mater. 69 (2022) 387–394.
[33] Z. Yuan, H. Wang, R. Li, J. Mao, H. Gao, Anti-Corros. Methods Mater. 70 (2023) 533–541.
[34] J.Y. Chen, Q. Feng, L.M. Cao, Z.Q. Sun, Mater. Sci. Eng. A 528 (2011) 3791–3798.
[35] L. Zheng, C. Xiao, G. Zhang, B. Han, D. Tang, J. Alloys Compd. 527 (2012) 176–183.
[36] L. Zheng, C. Xiao, G. Zhang, G. Gu, D. Tang, Rare Met. 30 (2011) 410–413.
[37] Y. Yuan, X. Liu, G. Pu, T. Wang, D. Zheng, Constr. Build. Mater. 308 (2021) 125108.
[38] A. Tian, J. Ma, Z. Liu, G. Kong, J. Geng, X. Huang, G. Li, Materials 17 (2024) 5821.
[39] S. Zhang, T. Zhang, Y. He, D. Liu, J. Wang, X. Du, B. Ma, J. Alloys Compd. 789 (2019) 460–471.
[40] R.M. Pidaparti, R.K. Patel, Corros. Sci. 52 (2010) 3150–3153.
[41] J.D. Ramsay, H.E. Evans, D.J. Child, M.P. Taylor, M.C. Hardy, Corros. Sci. 154 (2019) 277–285.
[42] Q. Zhao, C. Guo, K. Niu, J. Zhao, Y. Huang, X. Li, J. Mater. Res. Technol. 12 (2021) 1350–1359.
[43] N. Gong, T.L. Meng, S.L. Teo, J. Cao, C.J.J. Lee, C.K.I. Tan, D.C.C. Tan, A. Suwardi, M. Lin, R.D.K. Misra, H. Liu, Corros. Sci. 214 (2023) 111026.
[44] R. Yang, S. Han, X. Lei, J. Liu, J. Ma, J. Zhang, N. Wang, Surf. Coat. Technol. 474 (2023) 130057.
[45] J. Ma, G. Kong, Z. Liu, L. Zhao, A. Tian, C. Liu, Y. Wang, J. Mater. Res. Technol. 37 (2025) 5412–5422.
[46] J. Wang, H. Xue, Y. Wang, Rare Met. 40 (2020) 616–625.
[47] D. Hou, H. Luo, Z. Pan, Q. Zhao, H. Cheng, X. Wang, J. Mater. Res. Technol. 32 (2024) 2867–2881.
[48] J. Tang, S. Ni, Q. Chen, X. Yang, L. Zhang, J. Alloys Compd. 698 (2017) 121–127.
[49] H. Chen, X. Wang, Y. Lv, Y. Yan, C. Ding, Y. Meng, M. Wang, H. Wu, Q. Yuan, A. Wu, J. Wang, Int. J. Hydrogen Energy 71 (2024) 930–936.
[50] B.S. Singu, S.E. Hong, K.R. Yoon, J. Ind. Eng. Chem. 62 (2018) 321–328.
[51] C.L. Zeng, W. Wang, W.T. Wu, Corros. Sci. 43 (2001) 787–801.
[52] M. Zhu, S. Zeng, H. Zhang, J. Li, B. Cao, Sol. Energy Mater. Sol. Cells 186 (2018) 200–207.
[53] L. Xue, Y. Ding, K.G. Pradeep, R. Case, H. Castaneda, M. Paredes, Corros. Sci. 208 (2022) 110625.
[54] F. Sui, T. An, S. Zheng, L. Chen, S. Li, Corros. Sci. 204 (2022) 110386.
[55] C. Arcos, J.A. Ramos-Grez, M. Sancy, I. La Fé-Perdomo, R. Setchi, C. Guerra, Corros. Sci. 226 (2024) 111656.
[56] Q. Fu, J. Xu, B. Wei, Q. Qin, L. Gao, Y. Bai, C. Yu, C. Sun, Int. J. Press. Vessel. Pip. 190 (2021) 104313.

[57] C. Peng, G. Cao, T. Gu, C. Wang, Z. Wang, C. Sun, J. Mater. Res. Technol. 19 (2022) 709–721.

[58] G.Y. Koga, N. Birbilis, G. Zepon, C.S. Kiminami, W.J. Botta, M. Kaufman, A. Clarke, F.G. Coury, J. Alloys Compd. 884 (2021) 161107.

[59] Y. Wang, X. Mu, J. Dong, A.J. Umoh, W. Ke, J. Mater. Sci. Technol. 76 (2021) 41–50.

[60] T. Balusamy, M. Jamesh, S. Kumar, T.S.N.S. Narayanan, Mater. Corros. 63 (2011) 803–806.

[61] Q. Zhao, H. Luo, Z. Pan, X. Wang, X. Li, Corros. Sci. 223 (2023) 111468.

[62] M. Isakhani-Zakaria, S.R. Allahkaram, H.A. Ramezani-Varzaneh, Corros. Sci. 157 (2019) 472–480.

[63] Q. Zhao, Z. Pan, X. Wang, H. Luo, Y. Liu, X. Li, Corros. Sci. 208 (2022) 110666.

[64] H.S. Klapper, N.S. Zadorozne, R.B. Rebak, Acta Metallurgica Sinica (english Letters) 30 (2017) 296–305.

[65] X. Nie, H. Liu, X. Zhou, D. Yi, B. Huang, Z. Hu, Y. Xu, Q. Yang, D. Wang, Q. Gao, Mater. Sci. Eng. A 651 (2016) 37–44.

[66] Y. Jiao, L.J. Huang, S.L. Wei, H.X. Peng, Q. An, S. Jiang, L. Geng, J. Mater. Sci. Technol. 35 (2019) 1532–1542.

[67] D. Liu, Z. Wen, Z. Yue, Mater. Sci. Eng. A 605 (2014) 215–221.

[68] W. Xuan, G. Song, F. Duan, Z. Xiao, W. Pan, Y. Zhang, C. Li, J. Wang, Z. Ren, Mater. Sci. Eng. A 803 (2021) 140729.

[69] H. Cai, J. Hou, Y.-A. Guo, J. Xing, L.-Z. Zhou, J. Mater. Res. Technol. 28 (2024) 3631–3640.

[70] J. Wang, L. Zhou, X. Qin, L. Sheng, J. Hou, J. Guo, Mater. Sci. Eng. A 553 (2012) 14–21.

[71] M.E. Kassner, in: *Fundamentals of Creep in Metals and Alloys (third Edition)*, Butterworth-Heinemann, Boston, 2015, https://doi.org/10.1016/B978-0-08-099427-7.00010-4.

[72] A. Ardell, C. Barrett, O. Sherby, Transaction of the Metallurgical Society of AIME 230 (1964) 200.

[73] Y. Zhang, D. Li, X. Li, X. Liu, S. Zhao, Y. Li, J. Mater. Sci. Technol. 126 (2022) 93–105.

[74] Q. Li, S. Tian, H. Yu, N. Tian, Y. Su, Y. Li, Mater. Sci. Eng. A 633 (2015) 20–27.

[75] R.R. Unocic, N. Zhou, L. Kovarik, C. Shen, Y. Wang, M.J. Mills, Acta Mater. 59 (2011) 7325–7339.

[76] C. Kim, J. Park, H.-U. Hong, J. Gu, Y. Song, J. Alloys Compd. 900 (2022) 163479.

[77] L. Zhang, Q. Yang, J. Chen, Q. Li, J. Chen, M. Zhang, C. Xiao, Mater. Sci. Eng. A 933 (2025) 148302.